Journal of
Materials Chemistry A

Accepted Manuscript

Volume 6
Number 12
28 March 2018
Pages 4883-5230

Journal of
Materials Chemistry A

Materials for energy and sustainability

rsc.li/materials-a

ISSN 2050-7488

**ROYAL SOCIETY
OF CHEMISTRY**

COMMUNICATION
Zhenhai Wen et al.
An electrochemically neutralized energy-assisted low-cost
acid-alkaline electrolyzer for energy-saving electrolysis
hydrogen generation

This is an Accepted Manuscript, which has been through the Royal Society of Chemistry peer review process and has been accepted for publication.

Accepted Manuscripts are published online shortly after acceptance, before technical editing, formatting and proof reading. Using this free service, authors can make their results available to the community, in citable form, before we publish the edited article. We will replace this Accepted Manuscript with the edited and formatted Advance Article as soon as it is available.

You can find more information about Accepted Manuscripts in the Information for Authors.

Please note that technical editing may introduce minor changes to the text and/or graphics, which may alter content. The journal's standard Terms & Conditions and the Ethical guidelines still apply. In no event shall the Royal Society of Chemistry be held responsible for any errors or omissions in this Accepted Manuscript or any consequences arising from the use of any information it contains.

**ROYAL SOCIETY
OF CHEMISTRY**

rsc.li/materials-a

ROYAL SOCIETY OF CHEMISTRY

Journal of Materials Chemistry A

PAPER

Glycerol oxidation assisted electrocatalytic nitrogen reduction: ammonia and glyceraldehyde co-production on bimetallic RhCu ultrathin nanoflakes nanoaggregates †

Juan Bai,[a,‡] Hao Huang,[b,‡] Fu-Min Li,[b] Yue Zhao,[a] Pei Chen,[a] Pu-Jun Jin,[a] Shu-Ni Li,[b] Hong-Chang Yao,[c] Jing-Hui Zeng[a] and Yu Chen*[,a]

As an alternative pathway for present nitrogen fixation methods, the electrocatalytic nitrogen reduction reaction (NRR) under ambient conditions represents an attractive approach for sustainable and economic development of chemistry and biology. In this work, we synthesize bimetallic RhCu ultrathin nanoflakes nanoaggregates (RhCu-BUNNs) with atomic thickness by facile hydrothermal method. For the NRR, bimetallic RhCu-BUNNs exhibit the better electrocatalytic activity than monometallic Rh ultrathin nanoflakes nanoaggregates (Rh-UNNs) because the introduction of Cu can effectively weak the competitive hydrogen evolution reaction (HER), which can achieve a high NH_3 yield rate (95.06 μg h^{-1} mg_{cat}^{-1}) at -0.2 V potential. Density functional theory (DFT) calculations suggest that the introduction of Cu can effectively lower the energy-demanding in the *NN reductive process, resulting in NRR activity enhancement. Meanwhile, RhCu-BUNNs also show excellent electrocatalytic activity and selectivity for the glycerol oxidation reaction (GOR). For the electrochemical NH_3 production, the sluggish anodic oxygen evolution reaction (OER) increases the overall electrolysis voltage. Herein, we replace anodic OER with GOR to assist the NRR using bifunctional RhCu-BUNNs electrocatalyst. Specifically, only 1.2 V whole voltage is required for electrochemical NH_3 production in the presence of glycerol, accompanying with the generation of valuable glyceraldehyde at anode. This work may provide a promising pathway to obtain both NH_3 and valuable organic chemicals with high efficiency and low cost.

1. Introduction

Ammonia (NH_3) plays an important role in both our planet ecology and human life, including synthetic fertilizers, explosives, resins and dyes.[1-7] Although nitrogen (N_2) is the most abundant gas in earth, the reduction of N_2 to NH_3 is a kinetically difficult and energetically unfavourable multi-step reaction because the N≡N triple bond is highly stable (940.95 kJ mol^{-1}).[8-11] And N_2 biofixation by Rhizobium bacteria can't satisfy the needs of our life. Up to now, Haber–Bosch process is widely used for industrial NH_3 production, which produces a lot of carbon dioxide (CO_2) emissions and suffers from a very low conversion efficiency (ca. 10–15%) due to the harsh reaction conditions (such as high pressure and high temperature) and the unfavorable chemical equilibrium.[12-19] So far, the electrochemical nitrogen reduction reaction (NRR) has proved particularly promising due to its low-

cost device, simple reactor design, low pollutant emission, and room temperature and atmospheric pressure operation.[20-24] Tremendous efforts have been dedicated to develop various electrocatalyst for fixing N_2 to NH_3, including precious metal nanomaterials (Ru,[25, 26] Rh,[27] Au,[28-30] and Pd,[31, 32] etc.), carbon nanomaterials (N-doped porous carbon[33] and B-doped graphene,[23] etc.), and transition metal oxides nanomaterials (Fe_2O_3,[8] MnO,[34] Mn_3O_4,[35] Cr_2O_3,[36, 37] and SnO_2,[38] etc.).

Among metal-based electrocatalysts, rhodium (Rh) electrocatalyst is situated in the zenith of the volcano diagram of Skulason according to the density functional theory analysis for NH_3 synthesis.[39] While most of the electrons in this system contribute to the hydrogen evolution reaction (HER) rather than NRR, resulting in the low faradaic efficiency.[27] To work out these thorny problems, constructing precious metal based polymetallic nanomaterials through introducing transition metal may raise the utilization rate of electrons for NRR.[40] In addition, introducing transition metal in the precious ones can reduce the amount of precious metal as well as facilitate the large-scale applications in industry.

Generally, NRR and oxygen evolution reaction (OER) are involved in electrochemical NH_3 production, and the whole electrolysis voltage is mainly determined by the OER. Unfortunately, the sluggish OER kinetics generally restrains the overall electrolysis rate, and requires a big overpotential to drive overall reaction.[41-47] Additionally, the anodic oxidation product (i.e., O_2) has less value and it will explode when it mixed with the hydrogen (H_2) produced at cathode. Recently, an efficient approach to replace OER with

[a] Key Laboratory of Macromolecular Science of Shaanxi Province, Key Laboratory of Applied Surface and Colloid Chemistry (MOE), Shaanxi Key Laboratory for Advanced Energy Devices, School of Materials Science and Engineering, Shaanxi Normal University, Xi'an 710062, China E-mail: ndchenyu@gmail.com (Y. Chen)
[b] School of Chemistry and Chemical Engineering, Shaanxi Normal University, Xi'an 710062, PR China.
[c] College of Chemistry and Molecular Engineering, Zhengzhou University, Zhengzhou 450001, PR China.
‡ J. Bai and H. Huang contributed equally to this work.
† Electronic Supplementary Information (ESI) available: Experimental details and additional physical characterization. See DOI: 10.1039/x0xx00000x

Journal of Materials Chemistry A Accepted Manuscript

small molecule electrooxidation reaction (such as hydrazine, alcohol, urea and primary amine) has been developed to assist electrochemical H_2 production in water splitting.[48-53] Unfortunately, less attention has been paid to introduce favorable small molecule oxidation reaction to boost electrochemical NH_3 production.

Glycerol (Scheme S1A), an abundant biomass, can be converted into many value-added products, such as dihydroxyacetone, glyceraldehyde, tartronic acid, glycolic acid, and glyceraldehyde (Scheme S1B). Inspired by glycerol fuel cells, the substituted anodic reaction such as glycerol oxidation reaction (GOR) may be a valuable and effective way to reduce the overall electrolysis voltage of electrochemical NH_3 production.[54, 55] In this work, bimetallic RhCu ultrathin nanoflakes nanoaggregates (RhCu-BUNNs) with atomic thickness were synthesized by facile hydrothermal method, which revealed excellent electrocatalytic activity for both NRR and GOR. After using RhCu-BUNNs as a bifunctional electrocatalyst to construct a two-electrode RhCu-BUNNs||RhCu-BUNNs electrolyzer, the electrolyzer could drive 10 mA cm^{-2} current density at only 1.2 V voltage for electrochemical NH_3 production in the presence of glycerol, accompanying with the generation of valuable glyceraldehyde at anode.

2. Experimental section

2.1. Reagents and Chemicals

Polyallylamine hydrochloride (average molecular weight 5000) was obtained from Nitto Boseki Co., Ltd. Rhodium (III) chloride hydrate ($RhCl_3 \cdot 3H_2O$), copper (II) chloride dihydrate ($CuCl_2$), potassium hydroxide (KOH), sodium borohydride ($NaBH_4$), phenol (C_6H_5OH), ethanol (C_2H_5OH) , trisodium citrate ($Na_3C_6H_5O_7$), sodium hydroxide (NaOH), sodium hypochlorite (NaClO), ammonium sulfate ($(NH_4)_2SO_4$) and formaldehyde solution (HCHO, 40%) were acquired from Aladdin Industrial Co. Pt black and Pd black were purchased from Alfa Aesar. Sodium nitroprusside ($C_5H_4FeN_6Na_2O_3$) was obtained from Energy Chemical.

2.2. Synthesis of RhCu-BUNNs and Rh-UNNs

Typically, $RhCl_3$ aqueous solution (0.3 mL, 0.05 M) and $CuCl_2$ aqueous solution (0.1 mL, 0.05 M) were added into polyallylamine hydrochloride solution (5 mL, 0.05 M). Then, 0.4 mL HCHO was injected in the mixture (pH 7.0). The mix-solution was transferred to a Teflon-lined stainless-steel autoclave (20 mL), and heated at 140 °C for 6 h. For comparison, monometallic Rh ultrathin nanoflakes nanoaggregates (Rh-UNNs) were also synthesized using the same method in the absence of $CuCl_2$. The obtained RhCu-BUNNs and Rh-UNNs were separated by centrifugation, and washed with CH_3COOH for 10 h.

2.3. Synthesis of Au nanocrystals

Typically, 2 mL of 0.05 g mL^{-1} $NaBH_4$ solution was slowly added into 15.0 mL of 0.1 M $HAuCl_4$ solution under stirring at room temperature. The generated Au nanocrystals were achieved by centrifugation and washed with Millipore water.

2.4. Electrochemical measurements

All experiments were performed in three-electrode or two-electrode system by CHI 660 D electrochemistry workstation. Saturated calomel electrode and graphite rod were used as the reference electrode and counter electrode. The electrocatalyst ink was prepared by dispersing 8 mg electrocatalyst into a mixture solution containing 1.4 mL water, 0.6 mL ethyl alcohol and 10 μL Nafion solution. Then, the working electrode was acquired by dropping 20 μL electrocatalyst ink on carbon cloth electrode (0.5×0.5 cm^2) and dried at 40 °C for 2 h. In all LSV curve, *iR* drop was not compensated using the CHI 660D electrochemistry workstation.

2.5. Detection of NH_3 and N_2H_4

The products NH_3 and N_2H_4 were detected by phenol-hypochlorite method and Watt and Chrisp (para-dimethy-lamino-benzaldehyde) methods after the electrochemical reduction reaction, respectively.[56-58] The detection calibration curves of colorimetric NH_3 and N_2H_4 in 0.1 M KOH and 0.001 M H_2SO_4 solution were shown in Fig. S1†, Fig. S2†, Fig. S3† and Fig. S4†.

2.6. Instruments

Transmission electron microscopy (TEM) images, high-angle annular dark-field scanning TEM (HAADF-STEM) image, EDX mapping and selected area electron diffraction (SAED) image were measured by a TECNAI G2 F20 transmission electron microscopy. Scanning electron microscopy (SEM, SU-8020 instrument) was used to analyze the shape. Atomic force microscopy (AFM) image was obtained from a Dimension Icon instrument. The composition of sample was obtained from the energy-dispersive X-ray (EDX) technique. X-ray photoelectron spectroscopy (XPS) measurements were analyzed by AXIS ULTRA spectrometer. X-Ray diffraction (XRD) was carried out on a DX-2700 X-ray diffractometer. The products of glycerol oxidation were determined by high-pressure liquid chromatography (HPLC) equipped with refractive index detectors. An Aminex HPX-87H column was used for product separation. The absorbance of solution was investigated by ultraviolet and visible spectroscopy (Shimadzu UV-3600U).

2.7. DFT calculation

Density functional theory (DFT) calculations of NRR at Rh-BUNNs and RhCu-BUNNs were computed by using Material studio within the local density approximation (LDA). The Brillouin zone was sampled with a 4 × 4 × 1 Monkhorst-Pack grid. The structure was fully optimized until the force on each atom is less than 10^{-3} eV/Å. To avoid periodic interaction, a vacuum layer of 30 Å was incorporated into the slabs. The free energy (G) was computed from G=E+ZPE − *TS.* (where E was the total energy, ZPE was the zero-point energy, and the entropy (S) of each adsorbed state were yielded from DFT calculation, whereas the thermodynamic corrections for gas molecules were from standard tables.)

3. Results and discussion

3.1. Characterization of RhCu-BUNNs.

Bimetallic RhCu ultrathin nanoflakes nanoaggregates (RhCu-BUNNs) were obtained by reducing $RhCl_3$ and $CuCl_2$ with HCHO in the presence polyallylamine hydrochloride (Scheme S2) at 140 °C for 6 h. SEM (Fig. 1A)
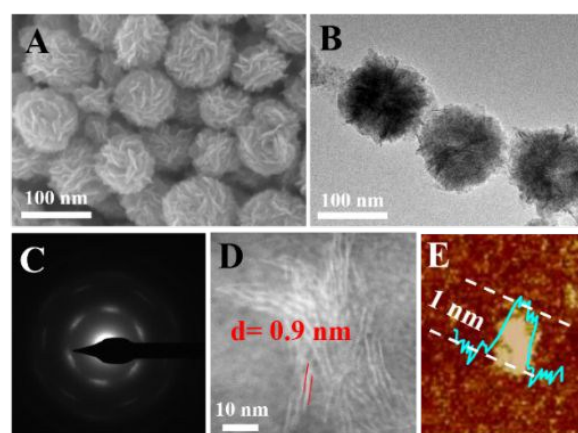

Fig. 1. (A) SEM image, (B) TEM image, (C) SAED pattern, (D) HAADF-STEM image, and (E) AFM image and height profile of RhCu-BUNNs.

Energy & Environmental Science　　　　　　　　　　　　　　　　**Paper**

and TEM (Fig. 1B) images show that RhCu-BUNNs have the three dimensionally (3D) dendritic structure, which are constructed of two-dimensional (2D) nanoflake subunits. And the average size of nanoaggregates is about 100 nm. SAED image of RhCu-BUNNs shows ring-like diffraction pattern, indicating their polycrystalline feature (Fig. 1C). In order to determine the thickness of nanoflake subunits, HAADF-STEM and AFM measurements were carried out. The luminous fringe-like region on HAADF-STEM image corresponds to nanoflakes perpendicular to the support substrate, which can be used to estimate the thickness of nanoflake subunits. The width of the luminous wire-like regions is ca. 0.9 nm (Fig. 1D), corresponding to the thickness of RhCu nanoflake subunits.[59] AFM image and height profile show that the thickness of the fallen RhCu-BUNNs nanoflake debris is about 1 nm (Fig. 1E), in consistent with the HAADF-STEM result.

The chemical composition of products is characterized by EDX spectrum, which shows the products contain the Rh and Cu elements, and the atomic ratio of Rh/Cu is ca. 3:1 (Fig. S5†). The XPS measurement is performed to investigate the surface composition and chemical state of RhCu-BUNNs. XPS analysis suggests that the Rh/Cu atomic ratio is 3:1 (Fig. S6†), which is coincident with EDX result. Rh 3d XPS analysis indicate that the percentage of metallic Rh is 96.1% (Fig. 2A), confirming the reduction of Rh^{III} precursor. The binding energy of Rh $3d_{5/2}$ at RhCu-BUNNs locates at 307.3 eV (Fig. 2A), showing a slight negative shift relative to that (307.5 eV) at monometallic Rh ultrathin nanoflakes nanoaggregates (Rh-UNNs) (Fig. S7†). This negative shift in binding energy indicates the modified electronic structure of Rh due to the formation of RhCu alloy, which originates from the electron donation from the Cu to Rh due to their discrepancy in electronegativity. Similarly, Cu 2p XPS analysis shows that metallic Cu is the predominant species (Fig. 2B), confirming the reduction of Cu^{II} precursor. X-Ray diffraction (XRD) measurement was performed to analysis the crystal phase and structure of RhCu-BUNNs. Regretfully, no obvious diffraction peaks are observe at RhCu-BUNNs (Fig. 2C), which in turn confirms ultrathin 2D structure of RhCu nanoflake subunits. Specifically, Son and co-workers also can't observed the valuable XRD information at ultrathin Rh nanoflakes with 1.5 nm thickness.[60] After annealing in Ar atmosphere at 600 °C for 3 h, RhCu-BUNNs clearly reveal the characteristic (111), (200), (220) and (311) diffraction peaks (Fig. S8†). And all diffraction peaks shift higher angel relative to the standard diffraction peaks of face center cubic Rh crystal, which confirms the alloy property of RhCu-BUNNs.

Fig. 2. (A) Rh 3d spectrum, (B) Cu 2p XPS spectrum, (C) XRD spectrum, and (D) HAADF-STEM-EDX mapping and line scanning profiles of RhCu-BUNNs.

The standard equilibrium potential of $RhCl_3/Rh$ couples (φ = 0.76 V) is much higher than that of Cu^{2+}/Cu couples (φ = 0.34 V). According to thermodynamic principle, Rh^{III} precursor will be preferentially reduced during the synthesis of RhCu-BUNNs. As a result, a Rh-rich core and a Cu rich shell type RhCu bimetallic nanostructures should be the main products in the reaction system. To visualize the chemical composition of RhCu-BUNNs, HAADF-STEM was performed. The HAADF-STEM image of single nanoaggregate shows the almost same luminance in whole pattern (Fig. 2D),[24] indicating that RhCu-BUNN have the alloy property rather than the core-shell structure.[61] The corresponding EDX mapping analysis reveal that Rh and Cu elements are homogeneously distributed in the nanoaggregate (Fig. 2D). The line-scan profiles across a single nanoaggregate show that Rh and Cu elements overlap completely (Fig. 2D), which further confirms the alloy property of RhCu-BUNN. In fact, monometallic Rh ultrathin nanoflakes nanoaggregates can be obtained by present hydrothermal method in the absence of Cu^{II} precursor (140 °C, 6 h).[59] But, the Cu^{II} precursor cannot be reduced in the absence of Rh^{III} precursor under the same experimental conditions (Fig. S9†). Thus, the formation of RhCu alloy can be ascribed to autocatalytic growth mechanism.[62] Concretely speaking, preferentially generated Rh crystal nuclei can promote the Cu^{II} reduction and newly-generated Cu atoms can entre preferentially generated Rh crystal nuclei by the interdiffusion mechanism due to thermodynamics factor, resulting in the formation of RhCu alloy. After increasing the amount of Cu^{II} precursor to Rh^{III}/Cu^{II}=2:1, the obtained products are mixture of RhCu-BUNN and Cu nanocrystals (Fig. S10†). As a result, the present RhCu-BUNNs with Rh/Cu atomic ratio of 3:1 are used in succedent electrocatalytic reactions.

3.2. The cathodic NRR at RhCu-BUNNs.

Prior to NRR measurement, the electrochemical active surface area (ECSA) of RhCu-BUNNs was calculated by measuring the hydrogen adsorption charge at cyclic voltammetry (CV) curve of RhCu-BUNNs in 0.5 M H_2SO_4 solution (Fig. S11†). By integrating the charge, the ECSA value of RhCu-BUNNs is calculated to be as high as 61.01 m^2 g^{-1}, which originates from the ultrathin nanoflakes structure of RhCu-BUNNs. Electrocatalytic NRR at RhCu-BUNNs tests were carried out in a three-electrode system using a two-compartment H-typed electrolytic cell (Fig. 3A). Linear sweep voltammetry (LSV) measurements of RhCu-BUNNs were carried out sequentially in Ar- and N_2-saturated 0.1 M KOH solution. As observed, the LSV curve of RhCu-BUNNs in N_2 atmosphere is different from that in Ar atmosphere (Fig. 3B), demonstrating RhCu-BUNNs have electrocatalytic activity for NRR. The NRR activity of RhCu-BUNNs was further evaluated by chronoamperometry tests at different applied potentials (Fig. 3C). After the chronoamperometry tests, phenolhypochlorite method was applied to detect the NH_3. The UV-Vis absorption spectra of the electrolytes stained with indophenol indicator are shown (Fig. S12†). The average NH_3 yield rate and corresponding faradaic efficiencies at different potentials are listed (Fig. 3D). As observed, the NH_3 yield rate increases with potential until -0.2, in which the NH_3 yield rate is calculated to be 95.06 μg h^{-1} mg_{cat}^{-1}. Meanwhile, no N_2H_4 is detected at all applied potentials (Fig. S13†), revealing the excellent selectivity of RhCu-BUNNs for NRR. Below -0.2 V potential, the mean NH_3 yield rate decreases, which is attributed to the competitive adsorption of N_2 and hydrogen species on Rh surface because the hydrogen species will preferentially occupy Rh active sites and impede the N_2 adsorption at Rh surface. In order to rule out the experimental error caused by the trace polyallylamine on RhCu-BUNNs surface, NRR experiment was also performed by giving the
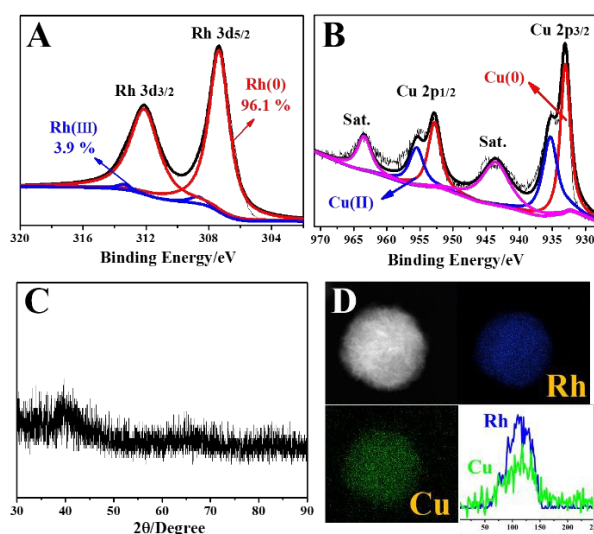
feeding gas of Ar. No NH_3 is observed in the cell of working electrode and absorbent, indicating the produced NH_3 come from N_2 rather than polyallylamine. Additionally, we noted that RhCu-BUNNs show higher NH_3 yield rate than most reported electrocatalysts under ambient conditions (Table 1), which in turn suggest the high NRR activity of RhCu-BUNNs.
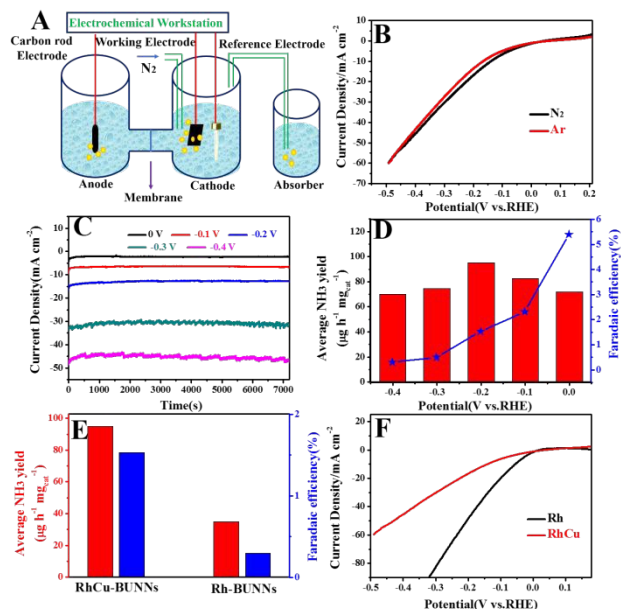

Fig. 3. (A) Schematic diagram for electrocatalytic NRR, (B) LSV curves of RhCu-BUNNs in N_2-saturated and Ar-saturated 0.1 M KOH solution at 5 mV s^{-1}, (C) Chronoamperometric curves of RhCu-BUNNs in N_2-saturated 0.1 M KOH solution at the corresponding potentials, (D) NH_3 yield rate and Faradaic efficiency of NRR at RhCu-BUNNs at each given potential, (E) NH_3 yield rate and Faradaic efficiency of NRR at RhCu-BUNNs and Rh-UNNs at -0.2 V potential, (F) LSV curves of RhCu-BUNNs and Rh-UNNs for HER in an Ar-saturated 0.1 M KOH solution.

Table 1 The NRR performance of recently reported electrocatalysts.

Catalysts	potential	NH_3 yield (μg h^{-1} mg$_{cat}$$^{-1}$)	Ref. (year)
RhCu-BUNNs	-0.2 V	95.06	This work
PdRu tripods	-0.2 V	37.23	2019[63]
S-doped graphene	-0.6 V	27.3	2019[64]
β-FeOOH nanorods	-0.75 V	23.32	2018[14]
Cr_2O_3 microspheres	-0.9 V	25.3	2018[36]
Nb_2O_5 nanofiber	-0.55 V	43.6	2018[65]
Ru single atoms	-0.2 V	120.9	2018[26]
Au/TiO_2 composites	-0.2 V	21.4	2017[30]
Pd/C	0.1 V	4.5	2018[31]
Au flowers	-0.2 V	25.57	2018[29]
Au_1/C_3N_4 composites	-0.1	1305	2018[66]
Mo_2N nanorods	-0.3	78.4	2018[67]
B_4C nanosheets	-0.75 V	26.57	2018[18]
Fe/Fe_3O_4 composites	-0.3 V	2.5	2018[68]
Cr_2O_3 nanofiber	-0.75 V	28.13	2018[37]

According to the correlation between total charge and total amount of NH_3 production,[27] the faradaic efficiency of RhCu-BUNNs for NRR is estimated to be 1.5% at -0.2 V potential (Fig. 3D), which is much higher than that of monometallic Rh nanosheets in our previous work (0.217%). To understand the role of Cu, we also investigated the electrocatalytic activity of monometallic Rh-UNNs for NRR. The NH_3 yield rate (95.06 μg h^{-1} mg$_{cat}$$^{-1}$) at RhCu-BUNNs is 2.7 folds higher than that (35 μg h^{-1} mg$_{cat}$$^{-1}$) at Rh-UNNs and faradaic efficiency of NRR (1.5%) at RhCu-BUNNs is much higher than that (0.3%) at Rh-UNNs counterparts (Fig. 3E). According to theoretical

calculation from Norskov,[39] Rh is the best precious metal electrocatalyst for nitrogen fixation. Francesc Illas's group explore the reactivity of RhCu alloys for H_2 dissociation by first principles-based density functional theory.[69] Their results indicate that the introduction of Cu atom can accelerate H_2 dissociation in an activated process due to structural effect and electronic effects, which is very similar to H_2 dissociation at PdCu alloy system.[40] Since the introduction of Cu can effectively accelerate the H_2 desorption from the precious metal surface, which undoubtedly increases the possibility of NRR. To verify this claim, the HER performance of RhCu-BUNNs and Rh-UNNs were investigated by LSV. HER activity of RhCu-BUNNs is much lower than that of Rh-UNNs (Fig. 3F), suggesting that the addition of Cu can weak HER and thus increase the faradaic efficiency of NRR.

In order to further investigate the influence of Cu on NRR activity of Rh-BUNNs, we performed DFT calculations to study the free-energy variation of NRR at Rh-BUNNs and RhCu-BUNNs. Similar to the case of HER, the surface of nanosheets appear to be electrocatalytically active site. The DFT calculations suggest that the surface of nanosheets plays the key role to activate the N_2 molecules. The free-energy profile of Rh-BUNNs show the potential-determining step (PDS) is the reductive protonation of adsorbed N_2, with a barrier of 0.71 eV (Fig. 4A). Favourably, the introduction of Cu can effectively lower the energy-demanding in the *NN reductive process on RhCu-BUNNs with a smaller barrier of 0.16 eV (Fig. 4B). Indeed, the opening of N≡N is the most energetically demanding step and the DFT results are in agreement with our experimental result. Herein, the relatively low barrier in the PDS on the RhCu-BUNNs predicts that RhCu-BUNNs is an more ideal electrocatalyst toward NRR than Rh-BUNNs.
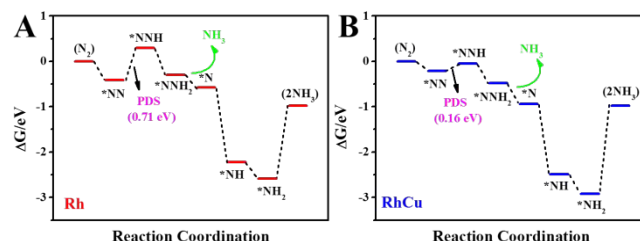

Fig. 4. Free-energy profile for NRR at (A) Rh-BUNNs and (B) RhCu-BUNNs active site.

The durability is another key criterion to evaluate the practicality of electrocatalyst. The current densities of NRR at RhCu-BUNNs at different potentials keep constant (Fig. 3C), revealing their excellent stability for NRR. After further performing the chronoamperometry of NRR at RhCu-BUNNs for continuous 25 h (Fig. S14†), no obvious current density decay is observed, indicating its excellent stability for NRR. Additionally, seven times recycling tests were carried out (Fig. S15†), no obvious variation in the NH_3 yield rate of RhCu-BUNNs was observed, further showing the excellent durability of RhCu-BUNNs. SEM images show RhCu-BUNNs also remains the initial morphology and structure after the long-term chronoamperometry (Fig. S16 †). The self-stability of RhCu-BUNNs was investigated by repeating CV scans in the range of 0-1.2 V at 50 mV s^{-1}. After 5000 CV cycles in 0.1 M KOH solution, the shape of CV curves only change slightly (Fig. S17 †). The previous works have indicated that Rh metal has extremely chemical inertness for harsh oxidation environment, resulting excellent self-stability of RhCu-BUNNs.[70, 71] Obviously, such outstanding self-stability contributes to excellent durability of RhCu-BUNNs for NRR.

3.3. Anodic GOR at RhCu-BUNNs

The electrocatalytic activity of RhCu-BUNNs for GOR was investigated by CV

in 0.1 M KOH solution containing 0.1 M glycerol (Fig. 5A). As observed, RhCu-BUNNs exhibit the obvious electrocatalytic activity for GOR. In the previous works, GOR have been investigated on Pt-based,[72] Pd-based[73, 74] and Au-based[75, 76] electrocatalyst. However, GOR on Rh-based electrocatalyst is rarely reported. Herein, we investigated the electrocatalytic activity of RhCu-BUNNs for GOR and compared with commercial Pt black, Pd black and Au nanocrystals by CV technique (Fig. 5B). Surprisingly, the peak potential of GOR at RhCu-BUNNs negatively shifts ca. 190, 420, and 640 mV compared to Pt black, Pd black, and Au nanocrystals, which indicates RhCu-BUNNs have super activity for GOR. Chronoamperometry test was performed to evaluate the durability of RhCu-BUNNs for GOR (Fig. 5C). During the whole process, the catalytic current remains stable at 0.8 V potential, indicating their outstanding durability. And EDX analysis further demonstrates the chemical composition of RhCu-BUNNs remain constant, indicating the stability of the catalyst during the oxidation reaction (Fig. S18†). After chronoamperometry test, HPLC analysis indicates that glyceraldehyde is the main oxidation product of glycerol, showing certain selectivity (Fig. S19†). In order to prove the GOR can replace the OER to decrease the potential of anode reaction, we perform LSV measurements in the presence and absence of glycerol using RhCu-BUNNs as electrocatalyst (Fig. 5D). In the absence of glycerol, the onset potential of OER at RhCu-BUNNs is about 1.50 V. After the addition of glycerol, the onset oxidation potential at RhCu-BUNNs sharply decreases to about 0.53 V, which is attributed to oxidation of glycerol.
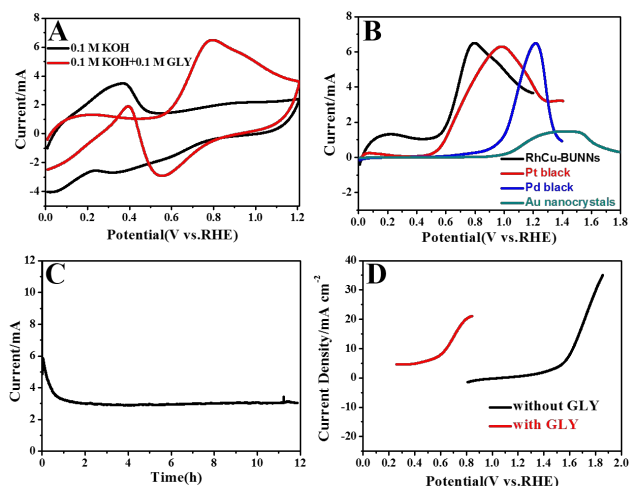

Fig. 5. (A) CV curve of RhCu-BUNNs in Ar-saturated 0.1 M KOH solution without and with 0.1 M glycerol at 50 mV s^{-1}, (B) CV curve of RhCu-BUNNs, Pt black, Pd black and Au nanocrystals in Ar-saturated 0.1 M KOH solution containing 0.1 M glycerol at 50 mV s^{-1}, (C) Chronoamperometric curve of RhCu-BUNNs in Ar-saturated 0.1 M KOH solution with 0.1 M glycerol at 0.8 V potential for 12 h, (D) LSV polarization curves of RhCu-BUNNs in 0.1 M KOH solution with and without 0.1 M glycerol.

3.4. GOR assisted NRR at bifunctional RhCu-BUNNs.

The above electrochemical measurements in three-electrode system have demonstrated that RhCu-BUNNs have outstanding electrocatalytic activity for both NRR at cathode and GOR at anode in KOH solution. So we built a two-electrode cell for GOR assisted NRR in 0.1 M KOH solution by using RhCu-BUNNs as both anode and cathode (i.e., RhCu-BUNNs||RhCu-BUNNs electrolyzer). In the presence of glycerol, RhCu-BUNNs||RhCu-BUNNs electrolyzer only needs overall voltage of 0.9 V to achieve current density of 10 mA cm^{-2}. In contrast, in the absence of glycerol, RhCu-BUNNs need overall voltage of 1.84 V to achieve current density of 10 mA cm^{-2}(Fig. 6A).

This fact indicates that GOR assisted NRR can afford higher energy conversion efficiency for electrochemical NH$_3$ production than conventional OER coupled NRR.

GOR assisted NH$_3$ production at bifunctional RhCu-BUNNs was performed by chronoamperometry test at 1.2 V potential in a two-electrode H-typed electrolyzer cell. RhCu-BUNNs were used as the anode to oxidize glycerol and cathode to generate NH$_3$, respectively. During the whole process, the gas bubbles are observed at RhCu-BUNNs cathode surface but no gas bubbles are observed at RhCu-BUNNs anode surface, indicating NRR and GOR occur simultaneously (Fig. 6B). After 12 h electrolysis, phenolhypochlorite determination method indicates that the NH$_3$ yield rate is about 92.01 μg h^{-1} mg$_{cat}$$^{-1}$ at cathodic cell. Meanwhile, HPLC spectrum demonstrates that glyceraldehyde is the main oxidation product of glycerol (Fig. S20†), which is consistent with the production the three-electrode system. Additionally, there is only slight current decrease over 12 h test period, further confirming its good stability of RhCu-BUNNs and revealing a promising potential for future practical application.
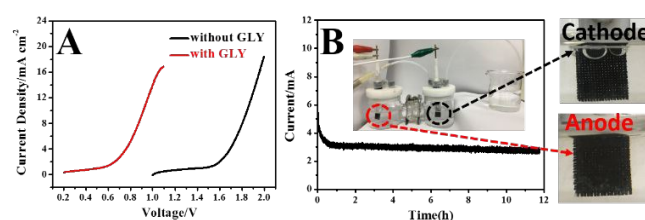

Fig. 6. (A) LSV polarization curves of RhCu-BUNNs||RhCu-BUNNs for the electrochemical NH$_3$ production in presence and absence of glycerol in 0.1 M KOH solution at 50 mV s^{-1}, (B) chronoamperometric curve of RhCu-BUNNs||RhCu-BUNNs at 1.2 V for 12 h and photograph of RhCu-BUNNs||RhCu-BUNNs water electrolyzer powered by 1.2 V applied voltage for GOR assisted NRR.

4. Conclusions

In summary, we demonstrate an energy-saving electrochemical NH$_3$ production by replacing the OER with electrooxidation conversion of glycerol into glyceraldehyde using bifunctional RhCu-BUNNs electrocatalyst, in which the bimetallic RhCu-BUNNs with ultrathin 2D nanoflake subunits play an important role in promoting their conversion reactions efficiently. Owing to the introduction of Cu, the competitive HER is weaken and thus the faradaic efficiency of NRR is increased. Meanwhile, the Cu introduction effectively lowers the energy-demanding in the *NN reductive process, resulting in NRR activity enhancement. Integrating with RhCu-BUNNs as an anode for GOR replacement of OER, the cell voltage is dramatically decreased. The assembled NRR/GOR electrolyzer system only requires a voltage of 1.2 V to drive overall electrolysis reaction. Additionally, the anodic substitution reaction avoids the KOH-consumption problem by CO$_2$, and benefits the industrial practicability. Our work opens up a new avenue to synchronously produce NH$_3$ at cathode and value-added organic chemicals at anode with high efficiency.

Acknowledgements

(GK201901002, GK201701007 and GK201902014), and the 111 Project (B14041).

Notes and references

1. S. L. Foster, S. I. P. Bakovic, R. D. Duda, S. Maheshwari, R. D. Milton, S. D. Minteer, M. J. Janik, J. N. Renner and L. F. Greenlee, *Nat. Catal.*, 2018, **1**, 490-500.

2. X. Cui, C. Tang and Q. Zhang, *Adv. Energy Mater.*, 2018, **8**, 1800369.

3. Y. Song, D. Johnson, R. Peng, D. K. Hensley, P. V. Bonnesen, L. Liang, J. Huang, F. Yang, F. Zhang, R. Qiao, A. P. Baddorf, T. J. Tschaplinski, N. L. Engle, M. C. Hatzell, Z. Wu, D. A. Cullen, H. M. Meyer, III, B. G. Sumpter and A. J. Rondinone, *Sci. Adv.*, 2018, **4**, e1700336.

4. L. Han, X. Liu, J. Chen, R. Lin, H. Liu, F. Lue, S. Bak, Z. Liang, S. Zhao, E. Stavitski, J. Luo, R. R. Adzic and H. L. Xin, *Angew. Chem. Int. Edit.,* 2019, **58**, 2321-2325.

5. H. Tao, C. Choi, L.-X. Ding, Z. Jiang, Z. Hang, M. Jia, Q. Fan, Y. Gao, H. Wang, A. W. Robertson, S. Hong, Y. Jung, S. Liu and Z. Sun, *Chem*, 2019, **5**, 204-214.

6. S. Wang, F. Ichihara, H. Pang, H. Chen and J. Ye, *Adv. Funct. Mater.*, 2018, **28**, 1803309.

7. M. Wang, S. Liu, T. Qian, J. Liul, J. Zhou, H. Ji, J. Xiong, J. Zhong and C. Yan, *Nat. Commun.*, 2019, **10**, 341.

8. X. Cui, C. Tang, X.-M. Liu, C. Wang, W. Ma and Q. Zhang, *Chem.–Eur. J.*, 2018, **24**, 18494-18501.

9. T. J. Sherbow, E. J. Thompson, A. Arnold, R. I. Sayler, R. D. Britt and L. A. Berben, *Chem.–Eur. J.,* 2019, **25**, 454-458.

10. F. Zhou, L. M. Azofra, M. Ali, M. Kar, A. N. Simonov, C. McDonnell-Worth, C. Sun, X. Zhang and D. R. MacFarlane, *Energ. Environ. Sci.*, 2017, **10**, 2516-2520.

11. A. J. Martin, T. Shinagawa and J. Perez-Ramirez, *Chem*, 2019, **5**, 263-283.

12. C. Guo, J. Ran, A. Vasileff and S.-Z. Qiao, *Energ. Environ. Sci.*, 2018, **11**, 45-56.

13. N. Cao and G. Zheng, *Nano Res.*, 2018, **11**, 2992-3008.

14. X. Zhu, Z. Liu, Q. Liu, Y. Luo, X. Shi, A. M. Asiri, Y. Wu and X. Sun, *Chem. Commun.*, 2018, **54**, 11332-11335.

15. R. Zhang, Y. Zhang, X. Ren, G. Cuo, A. M. Asiri, B. Zheng and X. Sun, *ACS Sustain. Chem. Eng.*, 2018, **6**, 9545-9549.

16. Y. Wang, X. Cui, J. Zhao, G. Jia, L. Gu, Q. Zhang, L. Meng, Z. Shi, L. Zheng, C. Wang, Z. Zhang and W. Zheng, *ACS Catal.*, 2019, **9**, 336-344.

17. B. H. R. Surrnto, D. Wang, L. M. Azofra, M. Harb, L. Cavallo, R. Jalili, D. R. G. Mitchell, M. Chatti and D. R. MacFarlane, *ACS Energy Lett.*, 2019, **4**, 430-435.

18. W. Qiu, X. Y. Xie, J. Qiu, W. H. Fang, R. Liang, X. Ren, X. Ji, G. Cui, A. M. Asiri, G. Cui, B. Tang and X. Sun, *Nat. Commun.*, 2018, **9**, 3485.

19. Y. Tang, Y. Kobayashi, N. Masuda, Y. Uchida, H. Okamoto, T. Kageyama, S. Hosokawa, F. Loyer, K. Mitsuhara, K. Yamanaka, Y. Tamenori, C. Tassel, T. Yamamoto, T. Tanaka and H. Kageyama, *Adv. Energy Mater.*, 2018, **8**, 1801772.

20. S. Mukherjee, D. A. Cullen, S. Karakalos, K. Liu, H. Zhang, S. Zhao, H. Xu, K. L. More, G. Wang and G. Wu, *Nano Energy*, 2018, **48**, 217-226.

21. X. Zhang, R.-M. Kong, H. Du, L. Xia and F. Qu, *Chem. Commun.*, 2018, **54**, 5323-5325.

22. X. Yang, J. Nash, J. Anibal, M. Dunwel, S. Kattel, E. Stavitski, K. Attenkofer, J. G. Chen, Y. Yan and B. Xu, *J. Am. Chem. Soc.*, 2018, **140**, 13387-13391.

23. X. Yu, P. Han, Z. Wei, L. Huang, Z. Gu, S. Peng, J. Ma and G. Zheng, *Joule*, 2018, **2**, 1610-1622.

24. S. Xu, D. C. Ashley, H.-Y. Kwon, G. R. Ware, C.-H. Chen, Y. Losovyj, X. Gao, E. Jakubikova and J. M. Smith, *Chem. Sci.*, 2018, **9**, 4950-4958.

25. D. Wang, L. M. Azofra, M. Harb, L. Cavallo, X. Zhang, B. H. R. Suryanto and D. R. MacFarlane, *ChemSusChem*, 2018, **11**, 3416-3422.

26. Z. Geng, Y. Liu, X. Kong, P. Li, K. Li, Z. Liu, J. Du, M. Shu, R. Si and J. Zeng, *Adv. Mater.,* 2018, **30**, 1803498.

27. H. M. Liu, S. H. Han, Y. Zhao, Y.-Y. Zhu, X. L. Tian, J.-H. Zeng, J.-X. Jiang, B. Y. Xia and Y. Chen, *J. Mater. Chem. A*, 2018, **6**, 3211-3217.

28. Y. Yao, S. Zhu, H. Wang, H. Li and M. Shao, *J. Am. Chem. Soc.*, 2018, **140**, 1496-1501.

29. Z. Wang, Y. Li, H. Yu, Y. Xu, H. Xue, X. Li, H. Wang and L. Wang, *ChemSusChem*, 2018, **11**, 3480-3485.

30. M. M. Shi, D. Bao, B. R. Wulan, Y. H. Li, Y. F. Zhang, J. M. Yan and Q. Jiang, *Adv. Mater.*, 2017, **29**, 1606550.

31. J. Wang, L. Yu, L. Hu, G. Chen, H. Xin and X. Feng, *Nat. Commun.*, 2018, **9**, 1795.

32. F. Pang, Z. Wang, K. Zhang, J. He, W. Zhang, C. Guo and Y. Ding, *Nano Energy*, 2019, **58**, 834-841.

33. Y. Liu, Y. Su, X. Quan, X. Fan, S. Chen, H. Yu, H. Zhao, Y. Zhang and J. Zhao, *ACS Catal.*, 2018, **8**, 1186-1191.

34. Z. Wang, F. Gong, L. Zhang, R. Wang, L. Ji, Q. Liu, Y. Luo, H. Guo, Y. Li, P. Gao, X. Shi, B. Li, B. Tang and X. Sun, *Adv. Sci.*, 2019, **6**, 1801182.

35. X. Wu, L. Xia, Y. Wang, W. Lu, Q. Liu, X. Shi and X. Sun, *Small*, 2018, **14**, 1803111.

36. Y. Zhang, W. Qiu, Y. Ma, Y. Luo, Z. Tian, G. Cui, F. Xie, L. Chen, T. Li and X. Sun, *ACS Catal.*, 2018, **8**, 8540-8544.

37. H. Du, X. Guo, R.-M. Kong and F. Qu, *Chem. Commun.*, 2018, **54**, 12848-12851.

38. L. Zhang, X. Ren, Y. Luo, X. Shi, A. M. Asiri, T. Li and X. Sun, *Chem. Commun.*, 2018, **54**, 12966-12969.

39. E. Skulason, T. Bligaard, S. Gudmundsdottir, F. Studt, J. Rossmeisl, F. Abild-Pedersen, T. Vegge, H. Jonsson and J. K. Norskov, *Phys. Chem. Chem. Phys.*, 2012, **14**, 1235-1245.

40. M.-M. Shi, D. Bao, S.-J. Li, B.-R. Wulan, J.-M. Yan and Q. Jiang, *Adv. Energy Mater.*, 2018, **8**, 1800124.

41. J. Yang, Y. Xiao, Q. Zhao, G. Zhang, R. Wang, G. Teng, X. Chen, M. Weng, D. He, S. Mu, Y. Lin and F. Pan, *Nano Energy*, 2019, **59**, 443-452.

42. Y. Zhao, M. Luo, S. Chu, M. Peng, B. Liu, Q. Wu, P. Liu, F. M. F. de Groot and Y. Tan, *Nano Energy*, 2019, **59**, 146-153.

43. W. Li, S. Watzele, H. A. El-Sayed, Y. Liang, G. Kieslich, A. S. Bandarenka, K. Rodewald, B. Rieger and R. A. Fischer, *J. Am. Chem. Soc.*, 2019, **141**, 5926-5933.

44. S. Niu, W.-J. Jiang, Z. Wei, T. Tang, J. Ma, J.-S. Hu and L.-J. Wan, *J. Am. Chem. Soc.*, 2019, DOI: 10.1021/jacs.9b01214.

45. Y.-J. Wang, B. Fang, D. Zhang, A. Li, D. P. Wilkinson, A. Ignaszak, L. Zhang and J. Zhang, *Electrochem. Energy Rev.*, 2018, **1**, 1-34.

46. C. Hu, Y. Xiao, Y. Zou and L. Dai, *Electrochem. Energy Rev.*, 2018, **1**, 84-112.

47. H. Shen, T. Thomas, S. A. Rasaki, A. Saad, C. Hu, J. Wang and M. Yang, *Electrochem. Energy Rev.*, 2019, **2**, 252-276.

48. J. Y. Zhang, H. Wang, Y. Tian, Y. Yan, Q. Xue, T. He, H. Liu, C. Wang, Y. Chen and B. Y. Xia, *Angew. Chem. Int. Edit.*, 2018, **130**, 7775-7779.

49. Y. Huang, X. Chong, C. Liu, Y. Liang and B. Zhang, *Angew. Chem. Int. Edit.*, 2018, **57**, 13163-13166.

50. X. Zhao, L. Dai, Q. Qin, F. Pei, C. Hu and N. Zheng, *Small*, 2017, **13**, 1602970.

51. B. You, X. Liu, X. Liu and Y. Sun, *ACS Catal.*, 2017, **7**, 4564-4570.

52. B. You, X. Liu, N. Jiang and Y. Sun, *J. Am. Chem. Soc.*, 2016, **138**, 13639-13646.

53. B. You and Y. Sun, *Accounts Chem. Res.*, 2018, **51**, 1571-1580.

54. N. Benipal, J. Qi, Q. Liu and W. Li, *Appl. Catal. B-Environ.*, 2017, **210**, 121-130.

55. G. L. Caneppele, T. S. Almeida, C. R. Zanata, E. Teixeira-Neto, P. S. Fernandez, G. A. Camara and C. A. Martins, *Appl. Catal. B-Environ.*, 2017, **200**, 114-120.

56. D. Bao, Q. Zhang, F. L. Meng, H. X. Zhong, M. M. Shi, Y. Zhang, J. M. Yan, Q. Jiang and X. B. Zhang, *Adv. Mater.*, 2017, **29**, 1604799.

57. G. W. Watt and J. D. Chrisp, *Anal. Chem.*, 1952, **24**, 2006-2008.

58. L. Solorzano, *Limnol. Oceanogr.*, 1969, **14**, 799-801.

59. J. Bai, G.-R. Xu, S.-H. Xing, J.-H. Zeng, J.-X. Jiang and Y. Chen, *ACS Appl. Mater. Inter.*, 2016, **8**, 33635-33641.

60. K. Jang, H. J. Kim and S. U. Son, *Chem. Mater.*, 2010, **22**, 1273-1275.

61. W. Zhang, J. Yang and X. Lu, *Acs Nano*, 2012, **6**, 7397-7405.

62. M. Gong, G. Fu, Y. Chen, Y. Tang and T. Lu, *ACS Appl. Mater. Inter.*, 2014, **6**, 7301-7308.

63. H. Wang, Y. Li, C. Li, K. Deng, Z. Wang, Y. Xu, X. Li, H. Xue and L. Wang, *J. Mater. Chem. A*, 2019, **7**, 801-805.

64. L. Xia, J. Yang, H. Wang, R. Zhao, H. Chen, W. Fang, A. M. Asiri, F. Xie, G. Cui and X. Sun, *Chem. Commun.*, 2019, **55**, 3371-3374.

65. J. Han, Z. Liu, Y. Ma, G. Cui, F. Xie, F. Wang, Y. Wu, S. Gao, Y. Xu and X. Sun, *Nano Energy*, 2018, **52**, 264-270.

66. X. Wang, W. Wang, M. Qiao, G. Wu, W. Chen, T. Yuan, Q. Xu, M. Chen, Y. Zhang, X. Wang, J. Wang, J. Ge, X. Hong, Y. Li, Y. Wu and Y. Li, *Sci. Bull.*, 2018, **63**, 1246-1253.

67. X. Ren, G. Cui, L. Chen, F. Xie, Q. Wei, Z. Tian and X. Sun, *Chem. Commun.,* 2018, **54**, 8474-8477.

68. L. Hu, A. Khaniya, J. Wang, G. Chen, W. E. Kaden and X. Feng, *ACS Catal.,* 2018, **8**, 9312-9319.

69. S. González, C. Sousa, M. Fernández-García, V. Bertin and F. Illas, *J. Phys. Chem. B*, 2002, **106**, 7839-7845.

70 Y.-Q. Kang, Q. Xue, Y. Zhao, X.-F. Li, P.-J. Jin and Y. Chen, *Small*, 2018, **14**, 1801239.

71. J. Bai, S.-H. Han, R.-L. Peng, J.-H. Zeng, J.-X. Jiang and Y. Chen, *ACS Appl. Mater. Inter.*, 2017, **9**, 17195-17200.

72. S. Lee, H. J. Kim, E. J. Lim, Y. Kim, Y. Noh, G. W. Huber and W. B. Kim, *Green Chem.*, 2016, **18**, 2877-2887.

73. H. Xu, P. Song, C. Fernandez, J. Wang, M. Zhu, Y. Shiraishi and Y. Du, *ACS Appl. Mater. Inter.*, 2018, **10**, 12659-12665.

74. H. Xu, J. Wang, B. Yan, S. Li, C. Wang, Y. Shiraishi, P. Yang and Y. Du, *Nanoscale*, 2017, **9**, 17004-17012.

75. H. Xu, B. Yan, J. Wang, K. Zhang, S. Li, Z. Xiong, C. Wang, Y. Shiraishi, Y. Du and P. Yang, *J. Mater. Chem. A*, 2017, **5**, 15932-15939.

76. A. Villa, N. Dimitratos, C. E. Chan-Thaw, C. Hammond, L. Prati and G. J. Hutchings, *Accounts Chem. Res.*, 2015, **48**, 1403-1412.

Journal of Materials Chemistry A Accepted Manuscript

The constructed NRR/GOR couple electrolyzer merely only required 1.2 V voltage for electrochemical NH_3 production in the presence of glycerol.